Stability Analysis and Active Damping Design for Grid-Forming Converters in LC Resonant Grids

SHIYI LIU [1,2] **(Student Member, IEEE), HENG WU** [2] **(Senior Member, IEEE),**
XIONGFEI WANG [2,3] **(Fellow, IEEE), THEO BOSMA** [1] **, AND GANESH SAUBA** [1] **(Member, IEEE)**

[1]Energy System Group, DNV, 6812AR Arnhem, The Netherlands
[2]Department of Energy Technology, Aalborg University, 9220 Aalborg, Denmark
[3]Division of Electric Power and Energy Systems, KTH Royal Institute of Technology, 114 28 Stockholm, Sweden

CORRESPONDING AUTHORS: HENG WU; XIONGFEI WANG (e-mail: hew@energy.aau.dk; xwa@energy.aau.dk)

ABSTRACT In this article, a small-signal model of grid-forming (GFM) converters that takes into account the presence of ac shunt capacitors in the power grid is presented. It is revealed that the inclusion of shunt ac capacitors in GFM converters leads to the emergence of two new resonant peaks in the loop gain of the active power control (APC) loop, in addition to the fundamental-frequency resonant peak that was previously identified in literature. Further analysis based on the equivalent APC considering P/Q coupling has confirmed the same destabilization effect of ac shunt capacitors by introducing two extra resonant peaks. Based on the insight, it is suggested that the active damping control needs to be adapted to effectively dampen all three resonant peaks to ensure the stable operation of GFM converters. Finally, simulations and real-time simulations are carried out to corroborate the theoretical findings.

INDEX TERMS Active damping, grid-forming (GFM), power control, small-signal model, stability, voltage-source converters.

I. INTRODUCTION

Nowadays, renewable energy resources, such as wind and solar power, are increasingly developed and interfaced with power systems via power converters [1]. The multitimescale control dynamics of power converters pose new challenges to the stability of the power grid [2], [3]. To address these challenges, grid-forming (GFM) control has emerged as a promising solution to operating converters in weak grids. By controlling GFM converters as a voltage source instead of a current source, GFM converters can operate stably even at low short-circuit ratios (SCR) of the power grid [4].

According to [5], GFM converters maintain terminal voltage by regulating its reactive power and synchronize with the power grid by regulating the output active power. Therefore, it is essential to design active and reactive power control (RPC) loops to ensure the stable operation of GFM converters [6]. When GFM converters are connected to an inductive grid impedance with an inductor filter, it is discovered in [7]

and [8] that there is a resonant peak at the grid fundamental frequency in the loop gain of the active power control (APC), which can cause unstable operation of GFM converters [9]. Traditional approaches, such as the active damping technique using a virtual resistor with a high-pass filter (HPF), have been proposed to dampen this resonant peak [7], [10]. The guidelines for tuning the parameters of the virtual resistor and its associated HPF are described in [11].

In previous studies [8], [12], it has been noted that the APC of GFM with shunt capacitors at the point of common coupling (PCC) in ac grids exhibits multiple resonance peaks, as opposed to a single peak at the fundamental frequency. However, the implications of these additional resonance peaks on system stability and the development of suitable active damping control strategies have not been comprehensively explored [13], [14]. It is important to recognize that the impact of shunt ac capacitors might be insignificant when they are small and have a limited effect on the low-frequency
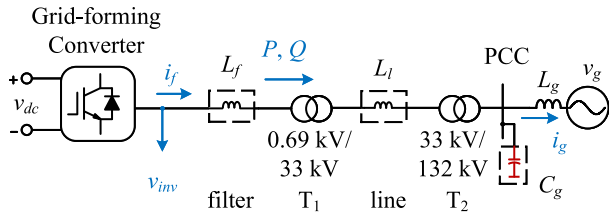
FIGURE 1. Configuration of the studied system consisting of a grid-forming voltage-source converter, filter, transformers, transmission/distribution lines, and infinite bus.

FIGURE 2. Structure of Grid-forming voltage-source converter.

dynamics of the APC, as elaborated in [8]. In scenarios involving large shunt ac capacitors (e.g., contributed by shunt capacitor branch utilized for reactive power compensation or capacitive loads), ignoring the influence of shunt ac capacitors in designing the active damping control may result in an inability to stabilize the GFM converter, as partly presented in our previous work [6]. Therefore, the primary contributions of this article are as follows.

1) Unlike prior studies that largely depended on numerical simulations or analysis, this work obtains the expressions for frequencies of resonance peaks, introduced by shunt ac capacitors, through the APC and the equivalent APC analysis.
2) Nevertheless, the influence of large inductors (e.g., contributed by transmission lines or transformers) and SCR in designing the active damping is specified, thereby delivering design recommendations for active damping control.
3) Moreover, the dynamic impact of the RPC loop is considered in the equivalent APC analysis to offer a deeper understanding of the dynamic impact of ac capacitors.

The rest of this article is organized as follows. In order to explore the dynamic effects of shunt ac capacitors on the GFM converter stability and the development of active damping control, this article establishes a small-signal model for GFM converters that includes shunt ac capacitors, as outlined in Section II. With the established model, an open-loop gain analysis is employed in Section III to examine the consequences of ac shunt capacitors and active damping on the stability of GFM converters. The investigation shows that incorporating shunt ac capacitors leads to two extra resonant peaks within the power control loops of GFM converters. By assessing the properties of these additional resonant peaks, the influence of shunt ac capacitors is analytically determined, and guidance for designing active damping control is offered in Section IV. Ultimately, simulation and real-time simulation evaluations are performed to substantiate the theoretical analysis, as detailed in Section V. Finally, Section VI concludes this article.

II. SMALL-SIGNAL MODELING
A. SYSTEM DESCRIPTION
Fig. 1 depicts the single-line diagram of a three-phase GFM converter [15]. The GFM converter is connected to the PCC
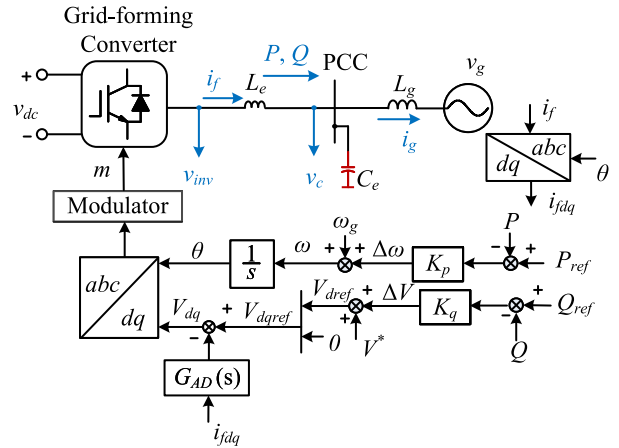
via a series of components, including an inductor filter L_f, step-up transformer T_1, distribution lines L_l, and step-up transformer T_2, where the grid impedance is represented by L_g, while C_g is the shunt ac capacitor, which may be contributed by shunt capacitor branches utilized for reactive power compensation or capacitive loads, and its stability impact is the main subject of investigation in this work.

The equivalent circuit of the three-phase GFM converter is shown in Fig. 2, and the equivalent inductance $L_e = L_f + L_{T1} + k_1^2 L_l + k_1^2 L_{T2}$, where k_1 and L_{T1} denote the transformation ratio and leakage inductance of transformer T_1, while k_2 and L_{T2} represent the transformation ratio and leakage inductance of transformer T_2. Meanwhile, the equivalent capacitor C_e can be calculated by $C_e = \frac{C_g}{k_1^2 k_2^2}$. v_{dc} refers to the constant dc voltage that is regulated by either a front-end converter which is connected to the dc-link or an energy storage unit [7]. The output active power, reactive power, the voltage of the converter bridge, and the voltage of the PCC are represented by P, Q, v_{inv}, and v_c, respectively. i_f represents the current of inductance L_e while i_g represents the grid current.

In this work, the GFM converter utilizes power synchronization control to synchronize with the power grid via the APC. This control method is commonly utilized and can be expressed, as [16]

$$\theta = \frac{1}{s}[\omega_g + K_p(P_{ref} - P)] \tag{1}$$

where P_{ref} is the active power reference and θ represents the angle reference. ω_g is the fundamental angular frequency of the grid, and K_p is the droop coefficient for the active power-frequency (P-f) control loop.

The reactive power-voltage (Q-V) droop control is adopted to adjust the reference of voltage magnitude, which is expressed as

$$V_{ref} = V^* + K_q(Q_{ref} - Q) \tag{2}$$

where the reference of reactive power and the voltage magnitude are denoted by Q_{ref} and V_{ref}, respectively. The nominal
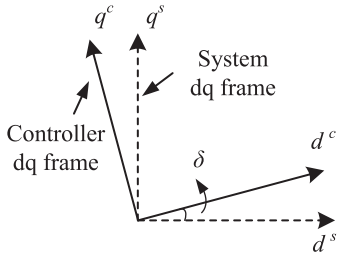
FIGURE 3. Controller *dq* frame and system *dq* frame.

voltage magnitude is represented by V^*, while K_q denotes the Q-V droop coefficient.

As shown in Fig. 2, the active damping with an HPF, given by $G_{AD}(s) = \frac{sk_v}{s+\omega_v}$, where ω_v is the cutoff frequency of the HPF, is further utilized to dampen the resonant peak of the APC of GFM converters [7].

Define x as a general state variable. Then real vectors are expressed by bold italic letters, for instance, $\boldsymbol{x}_{dq} = [x_d \quad x_q]^T$, where x_d and x_q represent the variable under d and q axis, respectively. The instantaneous active and reactive power can be described, as shown in (3). It is important to note that the factor 3/2 needs to be excluded from the model if the per unit (p.u.) value is used instead

$$\begin{bmatrix} P \\ Q \end{bmatrix} = \frac{3}{2} \begin{bmatrix} \boldsymbol{v}_{cdq}^T \boldsymbol{i}_{fdq} \\ \boldsymbol{v}_{cdq}^T \boldsymbol{J} \boldsymbol{i}_{fdq} \end{bmatrix} \tag{3}$$

where the matrix $\boldsymbol{J}$ is defined as

$$\boldsymbol{J} = \begin{bmatrix} 0 & -1 \\ 1 & 0 \end{bmatrix}. \tag{4}$$

B. SMALL-SIGNAL MODELING

The steady-state values of state variables are denoted by capital letters with subscript 0, for example, X_0. Conversely, the small-signal representations of state variables are signified with the hat symbol "^," such as $\hat{x}$.

The small-signal model of the GFM converter can be constructed by considering two rotating *dq* frames of the GFM converter [11]: 1) the controller-*dq* frame, defined by the output phase angle of the APC [17], and 2) the system-*dq* frame, aligned with the phase angle of the grid voltage, as illustrated in Fig. 3. For clarity, variables in the system-*dq* frame are indicated by the superscript *s*, while those in the controller-*dq* frame are denoted by the superscript *c*.

Define δ as the phase angle difference between the controller and the system *dq* frame, i.e., $\delta = \theta - \theta_g$, with θ_g set to zero. The relationships between the state variables in the controller *dq* frame ($\boldsymbol{x}_{dq}^c$) and the system *dq* frame ($\boldsymbol{x}_{dq}^s$) are then given by

$$\boldsymbol{x}_{dq}^c = \begin{bmatrix} \cos\delta & \sin\delta \\ -\sin\delta & \cos\delta \end{bmatrix} \boldsymbol{x}_{dq}^s. \tag{5}$$

Rewrite state variables with their corresponding steady-state values and small-signal perturbations, i.e., $x = X_0 + \hat{x}$,

we have,

$$\boldsymbol{i}_{dq} = \boldsymbol{I}_{dq0} + \hat{\boldsymbol{i}}_{dq}$$

$$\boldsymbol{v}_{dq} = \boldsymbol{V}_{dq0} + \hat{\boldsymbol{v}}_{dq}$$

$$\begin{bmatrix} \delta \\ V \end{bmatrix} = \begin{bmatrix} \delta_0 \\ V_0 \end{bmatrix} + \begin{bmatrix} \hat{\delta} \\ \hat{V} \end{bmatrix}$$

$$\begin{bmatrix} P \\ Q \end{bmatrix} = \begin{bmatrix} P_0 \\ Q_0 \end{bmatrix} + \begin{bmatrix} \hat{P} \\ \hat{Q} \end{bmatrix} \tag{6}$$

$$\sin(\delta_0 + \hat{\delta}) \approx \sin\delta_0 + \cos\delta_0\hat{\delta}$$

$$\cos(\delta_0 + \hat{\delta}) \approx \cos\delta_0 - \sin\delta_0\hat{\delta}.$$

By using (6) to replace the corresponding term in (5), the small-signal representation of the relationship between $\boldsymbol{x}_{dq}^s$ and $\boldsymbol{x}_{dq}^c$ can be expressed as

$$\hat{\boldsymbol{x}}_{dq}^c = \begin{bmatrix} \cos\delta_0 & \sin\delta_0 \\ -\sin\delta_0 & \cos\delta_0 \end{bmatrix} \hat{\boldsymbol{x}}_{dq}^s$$

$$- \hat{\delta} \underbrace{\begin{bmatrix} \cos\delta_0 & \sin\delta_0 \\ -\sin\delta_0 & \cos\delta_0 \end{bmatrix}}_{\boldsymbol{G}_{s0}} \begin{bmatrix} -X_{q0}^s \\ X_{d0}^s \end{bmatrix} \tag{7}$$

$$= \boldsymbol{G}_{s0}\hat{\boldsymbol{x}}_{dq}^s - \hat{\delta}\boldsymbol{G}_{s0} \begin{bmatrix} -X_{q0}^s \\ X_{d0}^s \end{bmatrix}.$$

By substituting the deviation equation, represented by (6), into the power equations given by (3), the small-signal model of the output active and reactive power can be formulated as follows:

$$\begin{bmatrix} \hat{P} \\ \hat{Q} \end{bmatrix} = \frac{3}{2} \left(\underbrace{\begin{bmatrix} \boldsymbol{I}_{fdq0}^T \\ -\boldsymbol{I}_{fdq0}^T\boldsymbol{J} \end{bmatrix}}_{\boldsymbol{I}_{f0}} \hat{\boldsymbol{v}}_{cdq}^s + \underbrace{\begin{bmatrix} \boldsymbol{V}_{cdq0}^T \\ \boldsymbol{V}_{cdq0}^T\boldsymbol{J} \end{bmatrix}}_{\boldsymbol{V}_{c0}} \hat{\boldsymbol{i}}_{fdq} \right). \tag{8}$$

According to the control diagram shown in Fig. 2, the dynamics of the converter output voltage in the controller *dq* frame can be expressed as
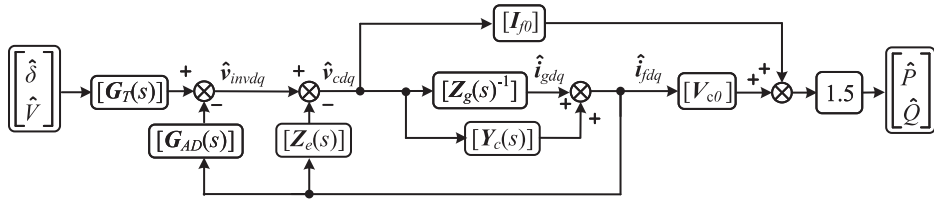
$$\hat{\boldsymbol{v}}_{invdq}^c = \hat{\boldsymbol{v}}_{invdqref}^c - \boldsymbol{G}_{AD}(s)\hat{\boldsymbol{i}}_{fdq}^c \tag{9}$$

where $\boldsymbol{G}_{AD}(s)$ represents the transfer function matrix of the active damping, which is expressed as

$$\boldsymbol{G}_{AD}(s) = \begin{bmatrix} G_{AD}(s) & 0 \\ 0 & G_{AD}(s) \end{bmatrix}. \tag{10}$$

By substituting (7) into (9), it can be reorganized as

$$\hat{\boldsymbol{v}}_{invdq}^c = \boldsymbol{G}_{s0}\hat{\boldsymbol{v}}_{invdq}^s - \hat{\delta}\boldsymbol{G}_{s0} \begin{bmatrix} -V_{invq0}^s \\ V_{invd0}^s \end{bmatrix}$$

$$= \hat{\boldsymbol{v}}_{invdqref}^c - \boldsymbol{G}_{AD}(s)\hat{\boldsymbol{i}}_{fdq}^c \tag{11}$$

$$= \hat{\boldsymbol{v}}_{invdqref}^c - \boldsymbol{G}_{AD}(s)\left(\boldsymbol{G}_{s0}\hat{\boldsymbol{i}}_{fdq}^s - \hat{\delta}\boldsymbol{G}_{s0} \begin{bmatrix} -I_{fq0}^s \\ I_{fd0}^s \end{bmatrix} \right).$$

FIGURE 4. Block diagram of a GFM converter with AC capacitors.

By using the result of (11), the small-signal representation of (9) in system dq frame can be derived as follows:

$$\hat{\boldsymbol{v}}_{\text{invdq}}^s = \underbrace{\begin{bmatrix} -V_{\text{invq0}} - \frac{sk_v}{s+\omega_v}I_{fq0} & \cos\delta_0 \\ V_{\text{invd0}} + \frac{sk_v}{s+\omega_v}I_{fd0} & \sin\delta_0 \end{bmatrix}}_{\boldsymbol{G}_T} \begin{bmatrix} \hat{\delta} \\ \hat{V} \end{bmatrix}$$

$$- \boldsymbol{G}_{\text{AD}}(s)\hat{\boldsymbol{i}}_{\text{fdq}}^s. \tag{12}$$

With the assumption of $\hat{\boldsymbol{v}}_{\text{gdq}}^s = 0$ and symmetrical three-phase system, the main circuit dynamics can be derived by applying the Kirchhoff's voltage law, as concluded from Fig. 2

$$\frac{d\hat{\boldsymbol{i}}_{\text{fdq}}^s}{dt} = \frac{\hat{\boldsymbol{v}}_{\text{invdq}}^s}{L_e} - \frac{\hat{\boldsymbol{v}}_{\text{cdq}}^s}{L_e} - \frac{R_e}{L_e}\hat{\boldsymbol{i}}_{\text{fdq}}^s + \omega_g \begin{bmatrix} \hat{i}_{fq}^s \\ -\hat{i}_{fd}^s \end{bmatrix}$$

$$\frac{d\hat{\boldsymbol{v}}_{\text{cdq}}^s}{dt} = \frac{1}{C_e}(\hat{\boldsymbol{i}}_{\text{fdq}}^s - \hat{\boldsymbol{i}}_{\text{gdq}}^s) + \omega_g \begin{bmatrix} \hat{v}_{cq}^s \\ -\hat{v}_{cd}^s \end{bmatrix} \tag{13}$$

$$\frac{d\hat{\boldsymbol{i}}_{\text{gdq}}^s}{dt} = \frac{\hat{\boldsymbol{v}}_{\text{cdq}}^s - R_g\hat{\boldsymbol{i}}_{\text{gdq}}^s}{L_g} + \omega_g \begin{bmatrix} \hat{i}_{gq}^s \\ -\hat{i}_{gd}^s \end{bmatrix}.$$

Applying the Laplace transformation to (13) [18], which leads to

$$\hat{\boldsymbol{v}}_{\text{invdq}}^s = \hat{\boldsymbol{v}}_{\text{cdq}}^s + \boldsymbol{Z}_e(s)\hat{\boldsymbol{i}}_{\text{fdq}}^s$$

$$\hat{\boldsymbol{i}}_{\text{fdq}}^s = \hat{\boldsymbol{i}}_{\text{gdq}}^s + \boldsymbol{Y}_c(s)\hat{\boldsymbol{v}}_{\text{cdq}}^s \tag{14}$$

$$\hat{\boldsymbol{v}}_{cdq}^s = \boldsymbol{Z}_g(s)\hat{\boldsymbol{i}}_{\text{gdq}}^s$$

where

$$\boldsymbol{Z}_e(s) = \begin{bmatrix} sL_e + R_e & -L_e\omega_g \\ L_e\omega_g & sL_e + R_e \end{bmatrix}$$

$$\boldsymbol{Y}_c(s) = \begin{bmatrix} sC_e & -C_e\omega_g \\ C_e\omega_g & sC_e \end{bmatrix} \tag{15}$$

$$\boldsymbol{Z}_g(s) = \begin{bmatrix} sL_g + R_g & -L_g\omega_g \\ L_g\omega_g & sL_g + R_g \end{bmatrix}$$

where R_e and R_g are the equivalent parasitic resistance and grid parasitic resistance, which are much smaller than the inductance ($R_g << L_g$ and $R_e << L_e$) [19].
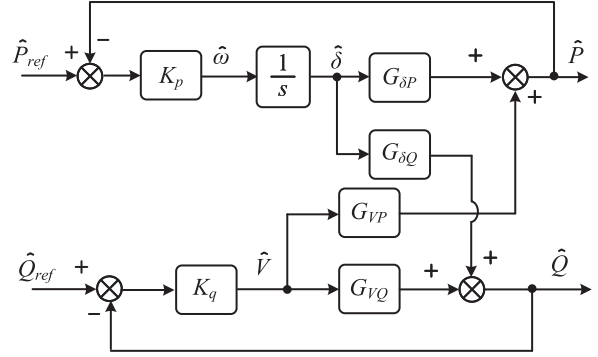
FIGURE 5. Small signal model of a GFM converter.

Based on (8) and (14), the transfer function matrix from $[\hat{\delta} \quad \hat{V}]^T$ to $[\hat{P} \quad \hat{Q}]^T$ can be derived, as the block diagram illustrated in Fig. 4. The corresponding detailed expressions are given in (16) shown at the bottom of this page, where $\boldsymbol{I}$ represents a unit 2×2 matrix. shown at the bottom of this page.

According to (1) and (2), the APC and RPC dynamics can be expressed as

$$\hat{\delta} = \frac{K_p}{s}(\hat{P}_{\text{ref}} - \hat{P})$$

$$\hat{V} = K_q(\hat{Q}_{\text{ref}} - \hat{Q}). \tag{17}$$

By combining (16) and (17), the complete small-signal model of a GFM converter can be described as shown in Fig. 5. Finally, the loop gain of APC and RPC loops of a GFM converter can thus be derived as given below,

$$T_{\delta P} = G_{\delta P}\frac{K_p}{s}$$

$$T_{\delta Q} = G_{\delta Q}\frac{K_p}{s}$$

$$T_{\text{VP}} = G_{\text{VP}}K_q \tag{18}$$

$$T_{\text{VQ}} = G_{\text{VQ}}K_q.$$

$$\begin{bmatrix} \hat{P} \\ \hat{Q} \end{bmatrix} = \underbrace{1.5\{\boldsymbol{I}_{g0} + \boldsymbol{V}_{c0}[\boldsymbol{Y}_c(s) + \boldsymbol{Z}_g^{-1}(s)]\}\{I + [\boldsymbol{Z}_e(s) + \boldsymbol{G}_{\text{AD}}(s)][\boldsymbol{Y}_c(s) + \boldsymbol{Z}_g^{-1}(s)]\}^{-1}\boldsymbol{G}_T(s)}_{\begin{bmatrix} G_{\delta P} & G_{\text{VP}} \\ G_{\delta Q} & G_{\text{VQ}} \end{bmatrix}} \begin{bmatrix} \hat{\delta} \\ \hat{V} \end{bmatrix} \tag{16}$$
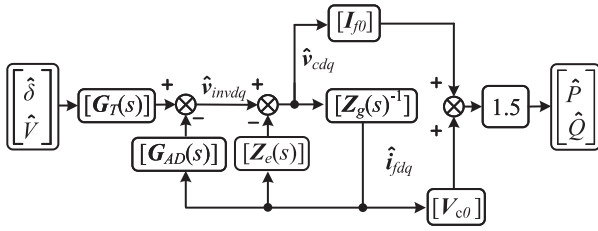
FIGURE 6. Block diagram of a GFM converter without AC capacitors.

For the condition that there is no shunt ac capacitor, the block diagram of a GFM converter is changed to Fig. 6, in which $\hat{\boldsymbol{i}}_{gdq} = \hat{\boldsymbol{i}}_{gdq} = \hat{\boldsymbol{i}}_{fdq}$, and transfer functions of the power plant for a GFM converter without ac capacitors are reduced to

$$\begin{bmatrix} \hat{P} \\ \hat{Q} \end{bmatrix} = 1.5\{\boldsymbol{I}_{g0} + \boldsymbol{V}_{c0}\boldsymbol{Z}_g^{-1}(s)\}$$

$$\cdot \underbrace{\{\boldsymbol{I} + [\boldsymbol{Z}_e(s) + \boldsymbol{G}_{AD}(s)]\boldsymbol{Z}_g^{-1}(s)\}^{-1}\boldsymbol{G}_T(s)}_{\begin{bmatrix} G'_{\delta P} & G'_{VP} \\ G'_{\delta Q} & G'_{VQ} \end{bmatrix}} \begin{bmatrix} \hat{\delta} \\ \hat{V} \end{bmatrix}. \quad (19)$$

III. SMALL-SIGNAL MODELING ANALYSIS

Fig. 5 clearly illustrates that the comprehensive small-signal model of a GFM converter presents multiple input and multiple output (MIMO) dynamics, exhibiting explicit coupling between the APC and RPC loops. To gain a deeper understanding of the dynamic impact of ac capacitors, the constant V_{ref} is assumed first when analyzing the open-loop gain of APC [7], [10]. The dynamic impact of RPC that modifies V_{ref} through the Q-V droop control will be reconsidered by deriving the equivalent loop gain of APC afterward.

A. APC GAIN ANALYSIS

Without active damping ($k_v = 0$), the poles of $T_{\delta P}$ can be calculated by solving (18) (R_e and R_g are ignored due to the small value [19])

$$\begin{cases} p_{1,2} = \pm j\omega_g \\ p_{3,4} = \pm j(\sqrt{\frac{L_e + L_g}{L_g L_e C_e}} + \omega_g) \\ p_{5,6} = \pm j(\sqrt{\frac{L_e + L_g}{L_g L_e C_e}} - \omega_g). \end{cases} \quad (20)$$

It is proven in previous studies [7] and [19] that only a pair of grid-fundamental-frequency resonant poles $p_{1,2} = \pm j\omega_g$ have been identified in the absence of shunt ac capacitors. Therefore, it is clear that the presence of shunt ac capacitors introduces two additional pairs of complex poles ($p_{3,4}$ and $p_{5,6}$), which results in the emergence of two extra resonant peaks in the APC, as illustrated in Fig. 7, where K_p is tuned at 0.2 p.u. to get a tradeoff between dynamic-response time and stability margin [20]. As expressed in (20), the frequencies of $p_{3,4}$ and $p_{5,6}$ are dependent on the values of L_g, L_e, and C_e.

As shown by the grey dash-dotted line, brown dashed line, and blue dotted line in Fig. 7, when C_e increases from 0.4 to
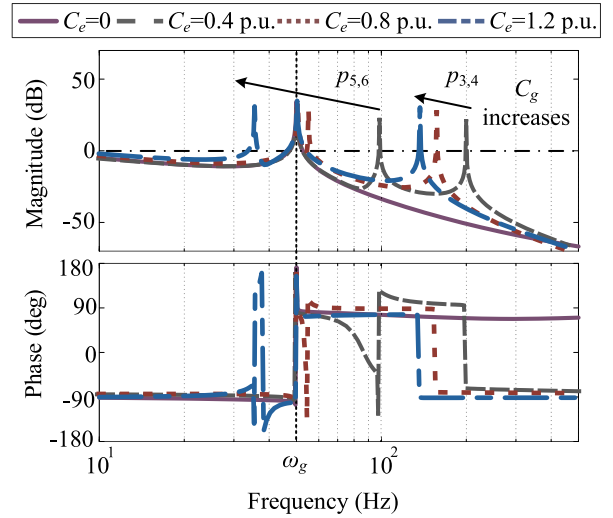

FIGURE 7. Bode plot of the APC with different AC shunt capacitors, $L_e = 0.5$ p.u., SCR = 1.5, without active damping.
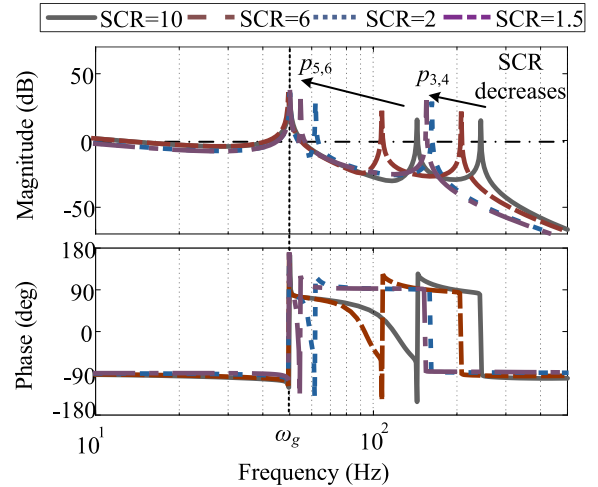

FIGURE 8. Bode plot of the APC with different SCR, $C_e = 0.8$ p.u., without active damping.

0.8 p.u. and 1.2 p.u., the frequency of $p_{3,4}$ decreases from 197.90 to 154.58 Hz and 135.39 Hz, respectively, whereas the frequency of $p_{5,6}$ decreases from 97.90 to 54.58 Hz and 35.39 Hz, respectively. Moreover, when there is no shunt ac capacitor, which means $C_e = 0$, there is only one resonant peak at 50 Hz in $T_{\delta P}$, as demonstrated by the purple solid line in Fig. 7.

On the other hand, the decreasing of SCR can also lower the frequencies of $p_{3,4}$ and $p_{5,6}$, as illustrated by the grey solid line, brown dashed line, blue dotted line, and purple dash-dotted line in Fig. 8. Specifically, when SCR decreases from 10 to 6, 2, and 1.5, the frequency of $p_{3,4}$ decreases from 243.65 to 208.11, 161.80, and 154.58 Hz, respectively, whilst the frequency of $p_{5,6}$ drops from 143.65 to 108.11, 61.80, and 54.58 Hz, respectively. Besides, it should be noted that the decreasing of SCR also results in a decrease of the bandwidth of the APC while $K_p = 0.2$ p.u.
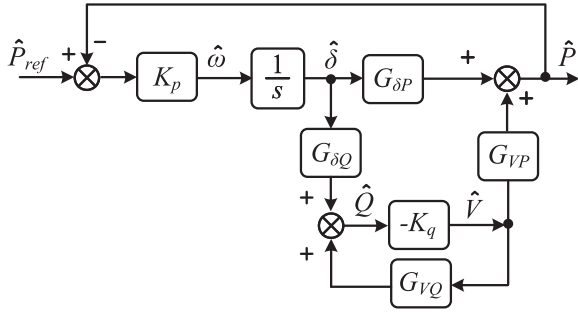
FIGURE 9. Equivalent APC block diagram of a GFM converter.

Based on the Bode plots in Figs. 7 and 8, it is evident that if $\sqrt{\frac{L_e+L_g}{L_gL_eC_e}} \approx 2\omega_g$ or $< 2\omega_g$, then the frequency of $p_{5,6}$ will be close to or lower than ω_g, while the frequency of $p_{3,4}$ will be higher than ω_g. In contrast, if this condition is not met, both $p_{3,4}$ and $p_{5,6}$ will have frequencies significantly higher than ω_g. The design of the active damping controller will be affected differently in these two scenarios, which will be elaborated in Section IV.

B. EQUIVALENT APC GAIN ANALYSIS

In order to further capture the impact of RPC, the equivalent loop gain of APC is derived based on Fig. 9. According to [21], the complete loop gain of the APC can be derived, as given in

$$T_{c\delta P} = (G_{\delta P} + G_{\text{coupled}})\frac{K_p}{s} \quad (21)$$

where

$$G_{\text{coupled}} = G_{\delta Q}\frac{-K_q}{1 + K_qG_{VQ}}G_{VP}. \quad (22)$$

Without active damping ($k_v = 0$), the Bode plots of the equivalent APC with different parameters (C_e and SCR) can be obtained by solving (21), as illustrated in Figs. 10 and 11.

As shown by the grey solid line in Fig. 10, it is obvious that the inclusion of ac shunt capacitors introduces two extra resonant peaks in $T_{c\delta P}$. When C_g increases, the frequencies of these two extra resonant peaks in $T_{c\delta P}$ decrease the same as those in $T_{\delta P}$. However, the magnitudes of resonant peaks at the frequencies of from 197.90 and 135.39 Hz in $T_{c\delta P}$, as illustrated by the brown dashed line and purple dotted line in Fig. 10, are notably lower in comparison to those in $T_{\delta P}$.

Meanwhile, when SCR decreases from 10 to 6, 2, and 1.5, the frequency of $p_{3,4}$ and $p_{5,6}$ also decreases in $T_{c\delta P}$, as shown by the grey solid line, brown dashed line, dark blue dotted line, and purple dash-dotted line in Fig. 11. Specifically, the frequency of $p_{3,4}$ drops from 243.65 to 208.11, 161.80 and 154.58 Hz, which is consistent with the observed trend in $T_{\delta P}$. On the other hand, the frequency of $p_{5,6}$ decreases from 144.10 to 109.25, 62.32, and 55.19 Hz, which is slightly higher than the frequencies observed in $T_{\delta P}$. In addition, the decrease of SCR also leads to a reduction in the bandwidth
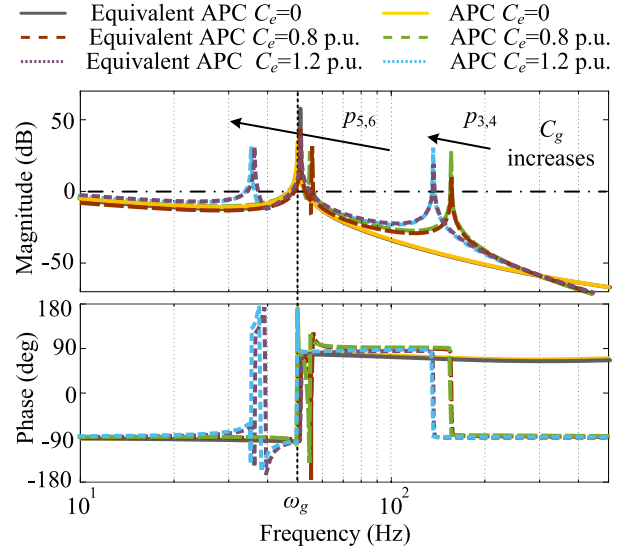
FIGURE 10. Bode plots of the APC and equivalent APC with different capacitors, $L_e = 0.5$ p.u., SCR = 1.5, without active damping.
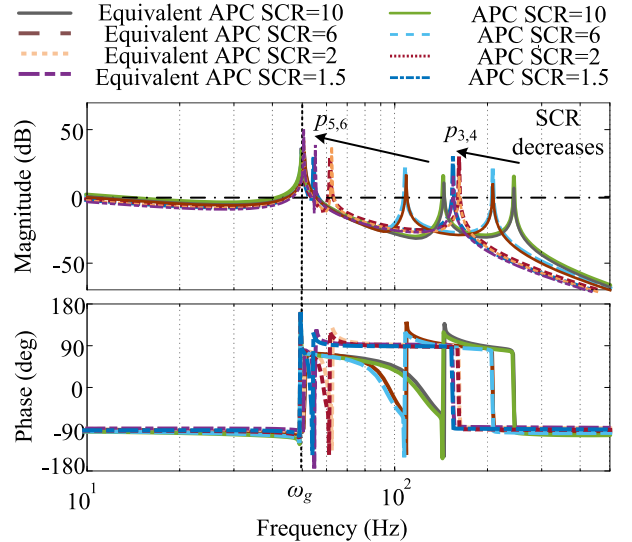
FIGURE 11. Bode plots of the APC and equivalent APC with different SCR, $C_e = 0.8$ p.u., without active damping.

of $T_{c\delta P}$, which aligns with the behavior and value observed in $T_{\delta P}$, as depicted in Fig. 8.

According to Figs. 10 and 11, it is evident that while the magnitudes and frequencies of some resonant peaks are slightly altered by taking P/Q coupling into account in the equivalent APC loop gain, the fundamental observation that the presence of shunt ac capacitors introduces two additional resonant peaks remains unchanged.

Furthermore, as illustrated in Figs. 12 and 13, it can be observed that changing the operation points, specifically by reducing the reference active power to half of its rated value, predominantly affects the amplitude of the resonance peaks, especially at the fundamental frequency. However, the
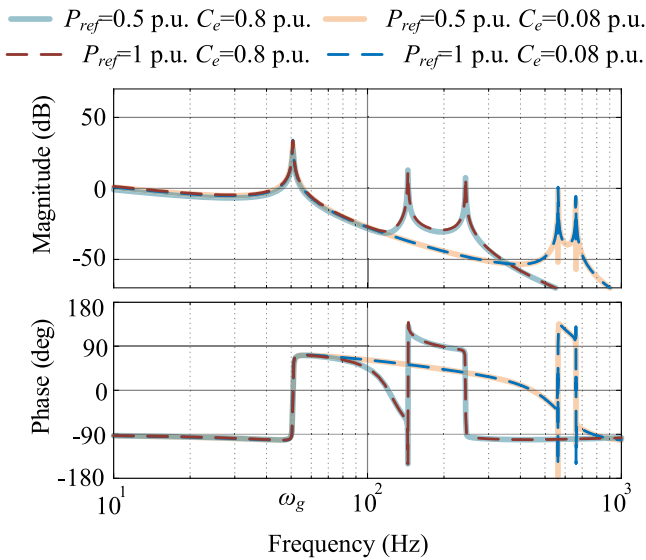
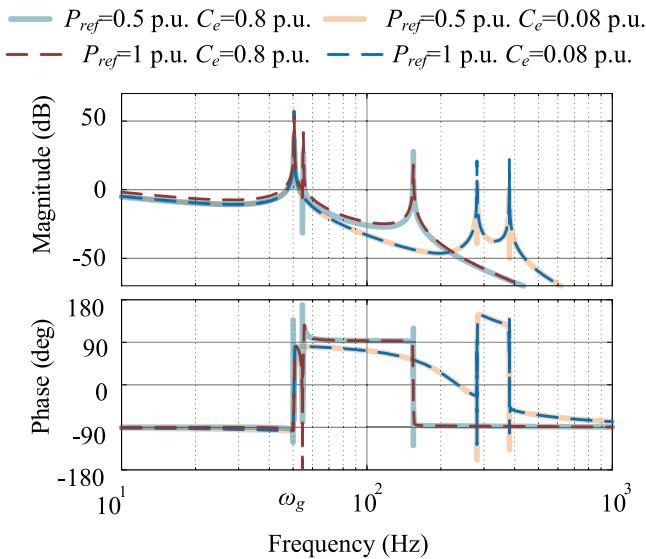FIGURE 12. Bode diagram of the equivalent APC with SCR = 10.

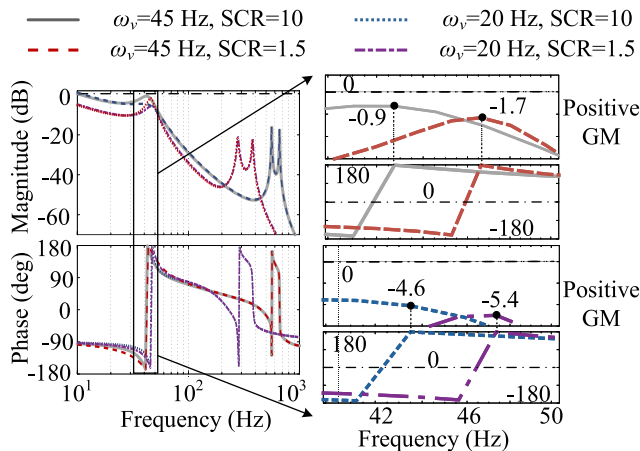FIGURE 13. Bode diagram of the equivalent APC with SCR = 1.5.

FIGURE 14. Bode diagram of the APC with active damping and C_e = 0.08 p.u.

frequency of these peaks remains unchanged since it is determined by the expression of $\sqrt{\frac{L_e+L_g}{L_gL_eC_e}}$ and ω_g, which are independent of operation points.

IV. ACTIVE DAMPING DESIGN

To ensure the stable operation of the GFM converter, the active damping resistor k_v is commonly utilized to dampen the resonant peaks in the APC, as discussed in [7]. In addition, as presented in Fig. 2, k_v is usually cascaded with an HPF $\frac{s}{s+\omega_v}$ to prevent its influence on the steady-state power control of the GFM converter.

The selection of the cutoff frequency, denoted as ω_v, for the HPF is essential since the effectiveness of active damping is limited to frequencies significantly higher than ω_v [11]. Therefore, the selection of ω_v should be based on the stability analysis approaches mentioned in Section III.

A. ACTIVE DAMPING DESIGN BASED ON APC GAIN ANALYSIS

As active damping demonstrates efficiency primarily at frequencies considerably above ω_v, this parameter should be determined in light of the lowest frequency of the resonant peaks in the APC, as illustrated by the Bode plots. In previous studies [7], it has been suggested that $\omega_v < \omega_g$ can effectively dampen the grid-frequency resonant peak in the APC transfer function, as shown by the purple solid line in Fig. 7. This is the only resonant peak present in the absence of shunt ac capacitors.

However, if shunt ac capacitors are present, this design guideline for ω_v must be revised due to the existence of two additional resonant peaks in the APC of a GFM converter system. It is therefore important to carefully consider the effect of shunt ac capacitors on the resonant peaks and select an appropriate value for ω_v to ensure effective active damping.

1) In situations where the shunt ac capacitor in the GFM converter is small, i.e., $\sqrt{\frac{L_e+L_g}{L_eL_gC_e}} >> 2\omega_g$, the frequencies of the complex poles $p_{3,4}$ and $p_{5,6}$ are considerably higher than ω_g and can be proficiently dampened by choosing $\omega_v < \omega_g$, as shown in Fig. 7. For example, in the case presented in Fig. 14, with $L_e = 0.5$ p.u., SCR $= 10/1.5$, and $C_e = 0.08$ p.u, the frequencies of the two additional resonant peaks are calculated to be 662.37 and 562.37 Hz, 380.72 and 280.72 Hz, respectively, which are well above 50 Hz. Therefore, all resonant peaks in the APC can be effectively dampened by selecting $\omega_v = 45$ Hz $< \omega_g$, and the system remains stable with a positive gain margin (GM) regardless of the change of SCR, as indicated in Fig. 14. In this case, the previous assumption in literature of ignoring the influence of ac capacitors when designing power control loops of GFM converter is justified [6].

2) If the value of $\sqrt{\frac{L_e+L_g}{L_eL_gC_e}}$ is close to $2\omega_g$, which corresponds to the case that GFM converter is connected to the grid with large C_e (introduced by the shunt capacitor utilized for reactive power compensation or the local capacitive load) or/and large L_e (introduced by the transmission line and
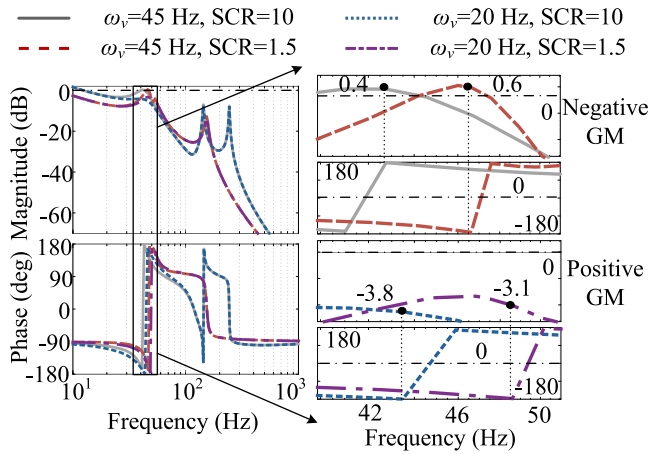
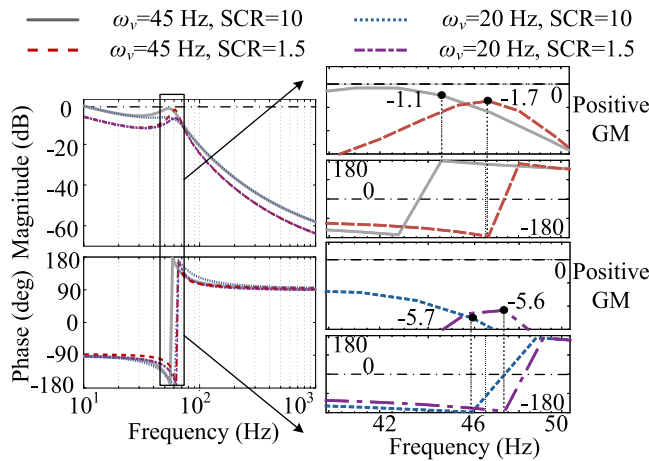**FIGURE 15.** Bode diagram of the APC with active damping and $C_e = 0.8$ p.u.

FIGURE 16. Bode diagram of the APC with active damping excluding shunt AC capacitor.

FIGURE 17. Bode diagram of the equivalent APC with active damping and $C_e = 0.08$ p.u.

TABLE 1. Parameters Used in the Simulation and Real-Time Simulation

Transformer T_1 inductance L_{T1} [15]	0.12 p.u.
Transformer T_2 inductance L_{T2}	0.15 p.u.
Transmission line inductance L_l	0.11 p.u.
Filter inductance L_f	0.12 p.u.
Equivalent inductance L_e	0.5 p.u.
Equivalent shunt ac capacitor C_e	0.8/0.08 p.u.
Equivalent resistance R_e	3.18e-3 p.u.
Grid resistance R_g	3.18e-3 p.u.
DC voltage V_{dc}	1150 V
Active power control parameter K_p	0.2 p.u.
Reactive power control parameter K_q	0.03 p.u.
Grid frequency ω_g	50 Hz
Switching frequency	5000 Hz.
Rated active power P_{ref}	3 MW
Active resistance k_v	0.14 p.u.

transformers). In this scenario, where the angular frequency of the complex poles $p_{5,6}$ (referred to as ω_{res1} henceforth) can become very close to or even lower than ω_g with low SCR, as presented in (20), selecting $\omega_v < \omega_g$ cannot effectively dampen the resonant peak. In such case, the impact of ac capacitors on the power control loop design of the GFM converter cannot be ignored, otherwise, the resonant peak at ω_{res1} cannot be identified correctly and there is a risk of destabilizing the system by choosing ω_v in the wrong range, which is demonstrated by an example presented in Fig. 15, with parameters given in Table 1. For instance, when SCR decreases from 10 to 1.5, the frequency of ω_{res1} decreases from 144.10 to 55.19 Hz, which is close to ω_g. Hence, the system can be stabilized by selecting ω_v for the worst-case scenario, particularly targeting the lowest frequency resonance condition. This method aligns with common industrial practices, where a range of SCR values is typically known or can be estimated based on similar systems or historical data [22].

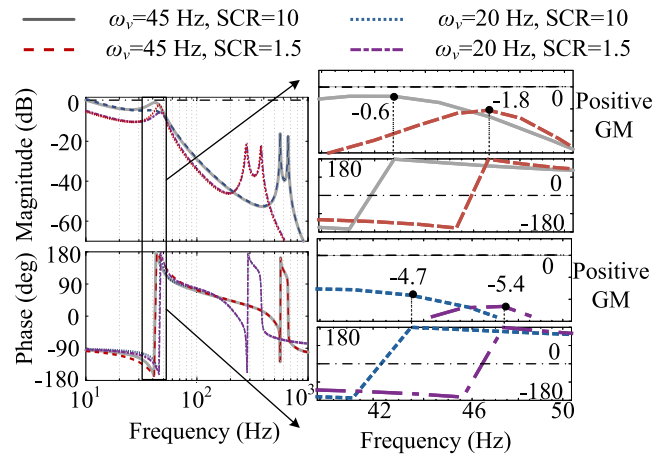The case study depicted in Fig. 15 illustrates that selecting $\omega_v = 45$ Hz $< \omega_g$ results in an unstable system with negative GM, independent of SCR variations. In contrast, selecting $\omega_v = 20$ Hz leads to a stable system, as demonstrated by the blue dotted line and purple dash-dotted line in Fig. 15. Nevertheless, disregarding the impact of the ac capacitor can lead to a misleading stability prediction since both $\omega_v = 20$ Hz and $\omega_v = 45$ Hz yield a stable loop gain regardless of the change in SCR, as shown in Fig. 16.

B. ACTIVE DAMPING DESIGN BASED ON EQUIVALENT APC GAIN ANALYSIS

As shown in Fig. 10, the RPC has no significant impact on the two additional resonant peaks introduced by shunt ac capacitors. Hence, in the cases of $L_e = 0.5$ p.u., $C_e = 0.08$ p.u., and SCR = 10/1.5, by selecting $\omega_v = 45$ Hz, the resonance peak at the frequency of $\omega_g = 50$ Hz in the equivalent APC gain can be dampened, as the grey solid line and brown dashed line shown in Fig. 17.

With $C_e = 0.8$ p.u., as demonstrated by Fig. 18, by still selecting $\omega_v = 45$ Hz $< \omega_g$, the system is unstable because of
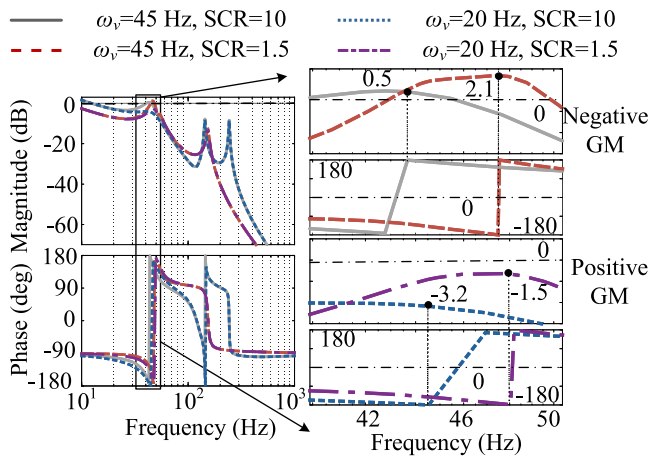
FIGURE 18. Bode diagram of the equivalent APC with active damping and $C_e = 0.8$ p.u.
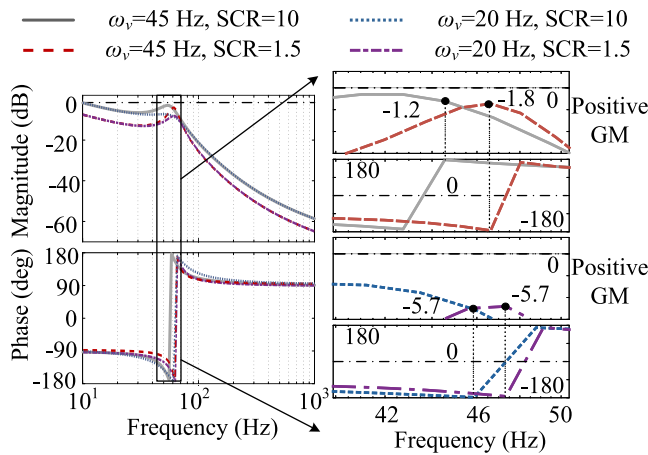
FIGURE 19. Bode diagram of the equivalent APC with active damping excluding shunt AC capacitor.

FIGURE 20. Comparison of step responses of P from Simulink model, the APC gain and equivalent APC gain analytical model.

FIGURE 21. Simulation results for active power with different capacitors when SCR = 10.

FIGURE 22. Simulation results for active power with different capacitors when SCR = 1.5.

the negative GM of the equivalent APC gain, whilst the system can be stabilized when $\omega_v = 20$ Hz. On the other hand, as shown in Fig. 19, neglecting the effect of shunt ac capacitors leads to a stable loop gain for either $\omega_v = 20$ Hz or $\omega_v = 45$ Hz, resulting in a misleading stability prediction.

In conclusion, despite the difficulty in analytically calculating ω_{res1} after considering P/Q coupling in the equivalent APC loop gain, the fundamental observation that the presence of shunt ac capacitors introduces two additional resonant peaks and ω_{res1} can be close to or even lower than ω_g still holds. Therefore, to effectively stabilize the system when shunt ac capacitors are applied, it is crucial to select ω_v by considering the influence of shunt ac capacitors, which supports the findings of the APC open-loop gain analysis.

V. APPLICATION OF A GRID-FORMING WIND POWER PLANT

A. SIMULATION RESULTS

To validate the theoretical analysis, time-domain simulations were performed using MATLAB/Simulink and the
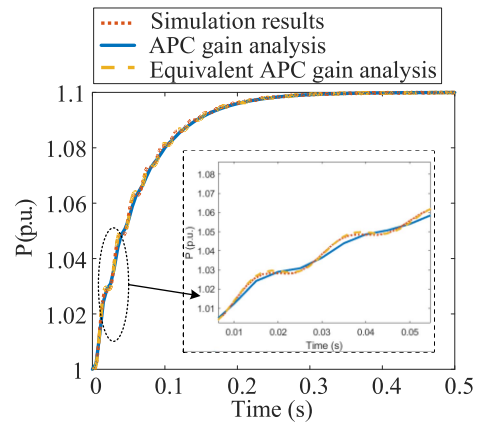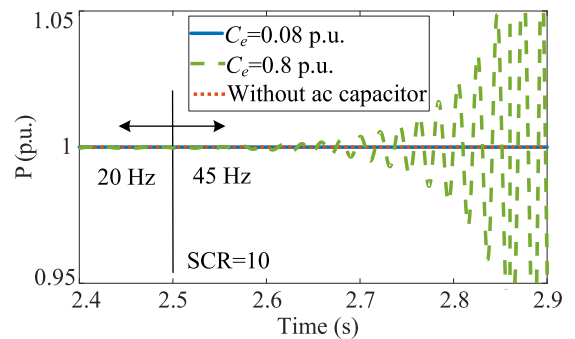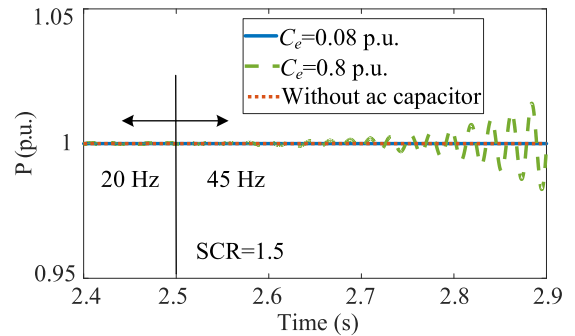
PLECS blockset, with the detailed electronic model shown in Fig. 2 [6]. The main parameters used in the simulations are listed in Table 1. The simulations allowed for a thorough examination of the system's behavior under various operating conditions and provided insight into the performance of the system. The results of the simulations were used to confirm the accuracy of the theoretical analysis and to guide the design of the real-time simulation setup.

Fig. 20 illustrates the responses in P for the case in Figs. 14 and 17 with $\omega_v = 45$ Hz to a 0.1 p.u. step disturbance in P_{ref} for the Simulink model, the APC gain, and the equivalent APC
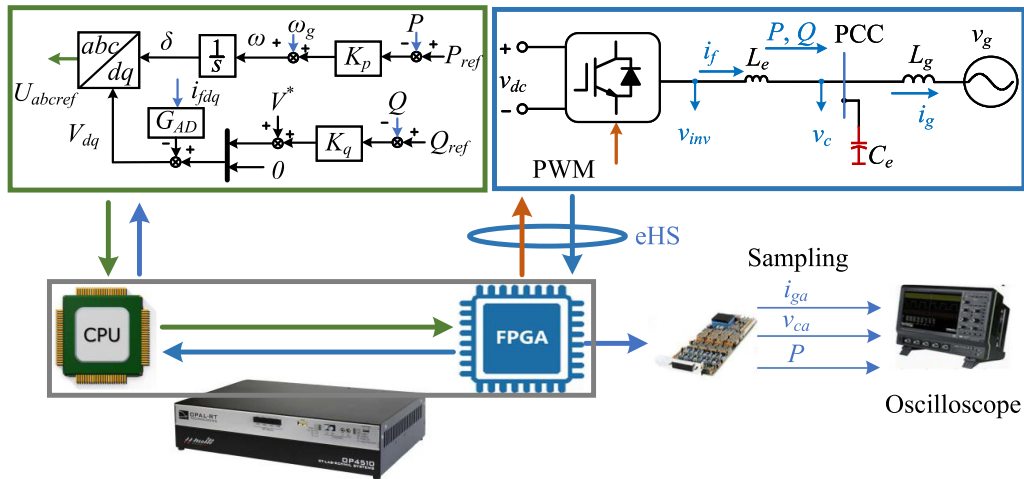
FIGURE 23. Real-time simulation set-up.

gain analytical model. As shown by the blue solid line, red dotted line, and yellow dashed line in Fig. 20, better matching between the equivalent APC gain analytical model and non-linear simulations is observed with a maximum error of 0.001 p.u., which is 20% of the maximum error between the APC gain analytical model and nonlinear simulations.

The simulation results for the active power when the frequency ω_v is varied from 20 to 45 Hz at 1.7 s are shown in Figs. 21 and 22. When the shunt capacitor $C_e = 0.8$ p.u. is connected to the PCC, as seen in Fig. 2, the system becomes unstable after the increase in ω_v. With SCR = 10, this instability is manifested in the form of a 46 Hz oscillation in the active power, which is in agreement with the stability prediction of the APC and equivalent APC gain analysis, as demonstrated in Figs. 15 and 18, while SRC = 1.5, a 49-Hz oscillation in the active power occurs, which is consistent with the stability prediction of the APC and equivalent APC gain analysis.

On the other hand, when there is no shunt ac capacitor or when a smaller capacitor C_e is used, the system is able to maintain stability with $\omega_v = 45$ Hz, as seen in Figs. 21 and 22. These results are consistent with the theoretical analysis presented in Fig. 14, 16, 17, and 19, which shows that the system is stable in the presence of a small shunt capacitor or the absence of a shunt capacitor regardless of the change of SCR.

Overall, the simulation results demonstrate that the shunt capacitor C_e can cause instability in the system when the frequency is changed, while the absence of a shunt capacitor or the use of a smaller capacitor can maintain stability. These results provide strong support for the validity of the theoretical analysis and guide the design of the real-time simulation setup.

B. REAL-TIME SIMULATION RESULTS

In this section, the three-phase grid-connected GFM converter is tested on a real-time simulation setup to prove its effectiveness, as shown in Fig. 23. To facilitate communication between the host development platform and the target publishing platform [23], the OPAL real-time emulator (OP4510) was employed [24]. The comprehensive architecture of OP4510, as given in [25] and [26], enabled the simulation of the hardware-in-the-loop configuration. The power circuits, which consisted of a three-phase converter connected to a grid via an *LC* network, were implemented using 4-core processors and a Kintex-7 410 T field programmable gate array (FPGA) by eHs solver with a time step of 2 us, as depicted in Fig. 23.

Subsequently, the central processing unit of OP4510 executes the control algorithm and generates reference signals by using RT-LAB, where the sampling time is 100 us. The reference signals were then transmitted to the internal pulsewidth modulation generator, running in the FPGA with a carrier frequency of 5 kHz. The 32 I/O digital and 16 analog I/O channels of OP4510 facilitated two-way communication with external devices, allowing the analog 0 channels to output the signals of v_{ca}, P, and i_{ga}, which were captured and displayed on an oscilloscope. The real-time simulation is designed with the same parameters as used in the simulation, which can be seen in Table 1.

The real-time simulation results presented in Fig. 24 are consistent with the simulation results. The system, which includes $C_e = 0.8$ p.u., resulting in ω_{res1} being close to ω_g as analyzed earlier, becomes unstable when ω_v changes from 20 to 45 Hz, as shown in Fig. 24(e) with SCR = 10 and Fig. 24(f) with SCR = 1.5. However, the system can remain stable without a shunt ac capacitor with SCR = 10 and 1.5, as illustrated in Fig. 24(a) and (b), or with a small ac capacitor, i.e., $C_e = 0.08$ p.u., leading to $\omega_{res1} >> \omega_g$, as depicted in Fig. 24(c) and (d) with SCR = 10 and 1.5.

Overall, the real-time simulation results are in good accordance with the simulated outcomes. The results demonstrate that the shunt ac capacitor C_e can lead to instability in the system when the frequency of HPF for active damping ω_v is determined solely on the basis of the fundamental frequency, without accounting for the impact of the ac shunt capacitors on system stability analysis. These findings lend
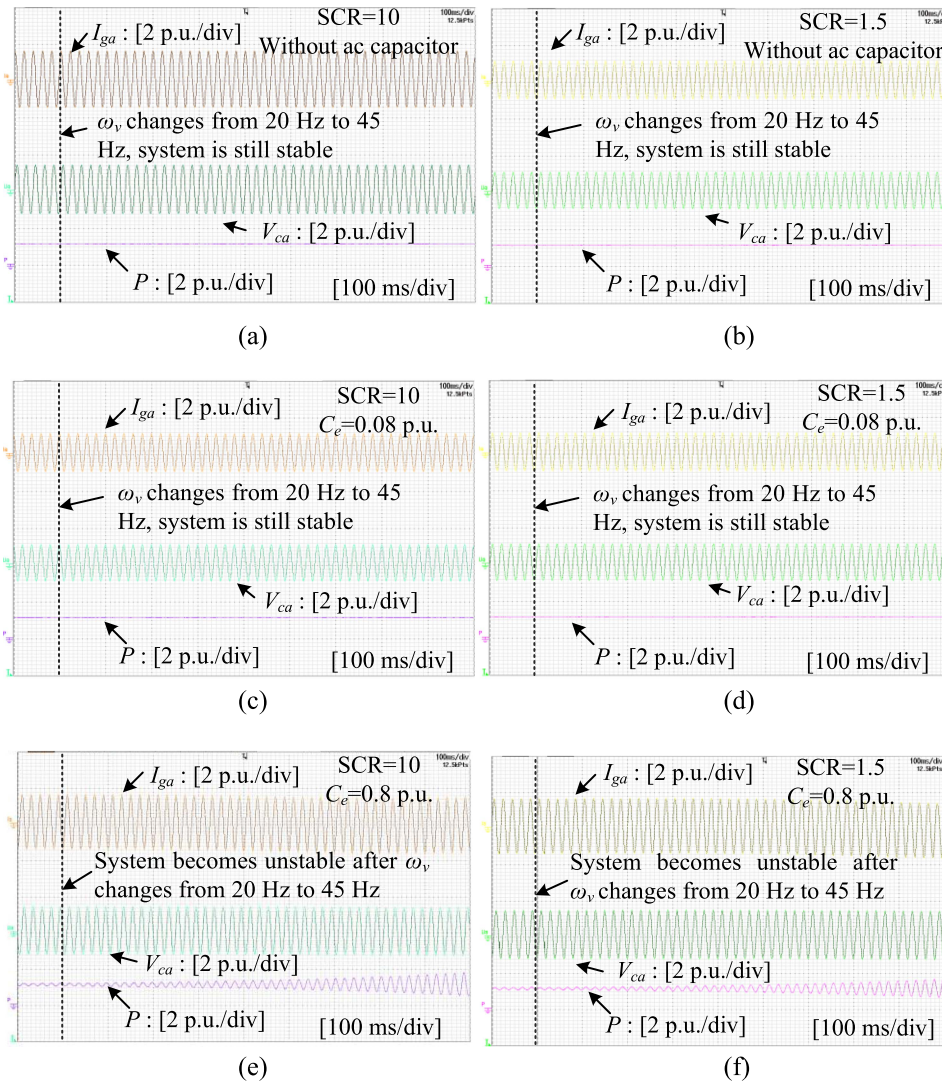
FIGURE 24. Real-time simulation results for active power. (a) Without shunt ac capacitors, SCR = 10. (b) Without shunt ac capacitors, SCR = 1.5. (c) C_e = 0.08 p.u., SCR = 10. (d) C_e = 0.08 p.u., SCR = 1.5. (e) C_e = 0.8 p.u., SCR = 10. (f) C_e = 0.8 p.u., SCR = 1.5.

strong support to the validity of the theoretical analysis performed.

VI. CONCLUSION

This article primarily focuses on investigating the effects of shunt ac capacitors on the stability of GFM converters. The goal is to understand how shunt ac capacitors influence the power control loop transfer functions. It is highlighted that two additional resonant peaks emerge in the loop gain of transfer functions for power control loops due to the integration of shunt ac capacitors. The study emphasizes that for large values of shunt capacitor C_e, the resonant frequency $\omega_{\mathrm{res1}} = \sqrt{\frac{L_e + L_g}{L_e L_g C_e}} - \omega_g$ can approach or even fall below the grid frequency ω_g, causing potential instability of the GFM inverter. To ensure stability, the selection of the HPF cutoff frequency used in the APC must take into account the value of ω_{res1}, as confirmed by the open-loop APC gain analysis

and equivalent APC gain analysis considering P/Q coupling. Furthermore, this article presents simulation and real-time simulation to validate the theoretical findings.

REFERENCES

[1] Y. Lin et al., "Research roadmap on grid-forming inverters," National Renewable Energy Lab. (NREL), Golden, CO, USA, NREL/TP-5D00-73476, 2020.

[2] D. Aragon, E. Unamuno, S. Ceballos, and J. Barrena, "Comparative small-signal evaluation of advanced grid-forming control techniques," *Electric Power Syst. Res.*, vol. 211, 2022, Art. no. 108154.

[3] X. Xiong, C. Wu, B. Hu, D. Pan, and F. Blaabjerg, "Transient damping method for improving the synchronization stability of virtual synchronous generators," *IEEE Trans. Power Electron.*, vol. 36, no. 7, pp. 7820–7831, Jul. 2021.

[4] J. Matevosyan et al., "Grid-forming inverters: Are they the key for high renewable penetration?," *IEEE Power Energy Mag.*, vol. 17, no. 6, pp. 89–98, Nov./Dec. 2019.

[5] H. Wu and X. Wang, "Virtual-flux-based passivation of current control for grid-connected VSCs," *IEEE Trans. Power Electron.*, vol. 35, no. 12, pp. 12673–12677, Dec. 2020.

[6] S. Liu et al., "Active damping of power control for grid-forming inverters in LC resonant grids," in *Proc. IEEE Energy Convers. Congr. Expo.*, 2022, pp. 1–6.

[7] L. Zhang, L. Harnefors, and H.-P. Nee, "Power-synchronization control of grid-connected voltage-source converters," *IEEE Trans. Power Syst.*, vol. 25, no. 2, pp. 809–820, May 2010.

[8] L. Zhang, L. Harnefors, and N. Johansson, "Power-system modeling—A transfer matrix approach," in *Proc. 11th IET Int. Conf. AC DC Power Transmiss.*, 2015, pp. 1–8.

[9] S. I. Nanou and S. A. Papathanassiou, "Grid code compatibility of VSC-HVDC connected offshore wind turbines employing power synchronization control," *IEEE Trans. Power Syst.*, vol. 31, no. 6, pp. 5042–5050, Nov. 2016.

[10] F. Zhao, X. Wang, Z. Zhou, Y. Sun, L. Harnefors, and T. Zhu, "Robust grid-forming control with active susceptance," *IEEE Trans. Power Electron.*, vol. 38, no. 3, pp. 2872–2877, Mar. 2023.

[11] L. Harnefors, M. Hinkkanen, U. Riaz, F. M. M. Rahman, and L. Zhang, "Robust analytic design of power-synchronization control," *IEEE Trans. Ind. Electron.*, vol. 66, no. 8, pp. 5810–5819, Aug. 2019.

[12] L. Zhang, L. Harnefors, and H.-P. Nee, "Modelling and control of VSC-HVDC connected to island systems," in *Proc. IEEE PES Gen. Meeting*, 2010, pp. 1–8.

[13] F. A. Alves, T. C. Tricarico, D. S. de Oliveira, G. C. Leal, B. W. França, and M. Aredes, "A procedure to design damping virtual impedance on grid-forming voltage source converters with LCL filters," *J. Control, Automat. Elect. Syst.*, vol. 33, no. 5, pp. 1519–1536, 2022.

[14] J. Wang, L. Chen, Z. Liu, Z. Zhang, and X. Zhang, "Optimized parameter design of the dual-loop control for grid-forming VSCs with LC filters," *IEEE Trans. Ind. Appl.*, vol. 58, no. 1, pp. 820–829, Jan./Feb. 2022.

[15] A. Avazov, "AC connection of wind farms to transmission system: From grid-following to grid-forming," Ph.D. dissertation, Faculty Eng. Sci., KU Leuven, Leuven, Belgium, 2022.

[16] J. Rocabert, A. Luna, F. Blaabjerg, and P. Rodríguez, "Control of power converters in AC microgrids," *IEEE Trans. Power Electron.*, vol. 27, no. 11, pp. 4734–4749, Nov. 2012.

[17] H. Wu and X. Wang, "Small-signal modeling and controller parameters tuning of grid-forming VSCs with adaptive virtual impedance-based current limitation," *IEEE Trans. Power Electron.*, vol. 37, no. 6, pp. 7185–7199, Jun. 2022.

[18] T. Suntio, T. Messo, and J. Puukko, *Power Electronic Converters: Dynamics and Control in Conventional and Renewable Energy Applications.*, Hoboken, NJ, USA: Wiley, 2017.

[19] D. Pan, X. Wang, F. Liu, and R. Shi, "Transient stability of voltage-source converters with grid-forming control: A design-oriented study," *IEEE Trans. Emerg. Sel. Topics Power Electron.*, vol. 8, no. 2, pp. 1019–1033, Jun. 2020.

[20] L. Zhang, "Modeling and control of VSC-HVDC links connected to weak ac systems," Ph.D. dissertation, School Elect. Eng., KTH, Stockholm, Sweden, 2010.

[21] H. Wu, "Small-signal and transient stability analysis of voltage-source converters," Ph.D. dissertation, Dept. Energy Technol., Aalborg Univ., Aalborg, Denmark, 2020.

[22] Y. Zhang, S.-H. F. Huang, J. Schmall, J. Conto, J. Billo, and E. Rehman, "Evaluating system strength for large-scale wind plant integration," in *Proc. IEEE PES Gen. Meeting Conf. Expo.*, 2014, pp. 1–5.

[23] N. A. Maged, H. M. Hasanien, E. A. Ebrahim, M. Tostado-Véliz, and F. Jurado, "Real-time implementation and evaluation of gorilla troops optimization-based control strategy for autonomous microgrids," *IET Renewable Power Gener.*, vol. 16, no. 14, pp. 3071–3091, 2022.

[24] W. Kang, M. Chen, W. Lai, and Y. Luo, "Distributed real-time power management for virtual energy storage systems using dynamic price," *Energy*, vol. 216, 2021, Art. no. 119069.

[25] S. K. Singh, B. P. Padhy, S. Chakrabarti, S. Singh, A. Kolwalkar, and S. M. Kelapure, "Development of dynamic test cases in OPAL-RT real-time power system simulator," in *Proc. 18th Nat. Power Syst. Conf.*, 2014, pp. 1–6.

[26] K.-R. Sorto-Ventura, M. Abarzadeh, K. Al-Haddad, and L. A. Dessaint, "23-level single DC source hybrid PUC (H-PUC) converter topology with reduced number of components: Real-time implementation with model predictive control," *IEEE Open J. Ind. Electron. Soc.*, vol. 1, pp. 127–137, 2020.